Effects of streamwise vortex breakdown on supersonic combustion

Toshihiko Hiejima*

Department of Aerospace Engineering, Osaka Prefecture University, 1-1 Gakuen-cho, Nakaku, Sakai, Osaka 599-8531, Japan

(Received 19 November 2015; revised manuscript received 2 February 2016; published 14 April 2016)

This paper presents a numerical simulation study of the combustion structure of streamwise vortex breakdown at Mach number 2.48. Hydrogen fuel is injected into a combustor at sonic speed from the rear of a hypermixer strut that can generate streamwise vortices. The results show that the burning behavior is enhanced at the points of the shock waves that are incident on the vortex and therefore the vortex breakdown in the subsonic region occurs due to combustion. The breakdown domain in the mainstream is found to form a flame-holding region suited to combustion and to lead to a stable combustion field with detached flames. In this way, streamwise vortex breakdown has an essential role in combustion enhancement and the formation of flames that hold under supersonic inflow conditions. Finally, the combustion property defined here is shown to coincide with the produced-water mass flow. This property shows that the amount of combustion is saturated at equivalence ratios over 0.4, although there is a slight increase beyond 1.

DOI: 10.1103/PhysRevE.93.043115

I. INTRODUCTION

Efficient combustion control in supersonic flows is important for realizing supersonic combustion ramjet (scramjet) engines for hypersonic air-breathing propulsion systems. Reducing the required length of the combustor associated with the engine weight is also necessary [1]. The main issue to address is effective fuel-oxidizer mixing in the engine over the short time scale of combustion. To achieve this, the best approach is thought to be to make use of vortical activities leading to turbulent diffusion. It follows therefore that understanding the relationship between vortical motion and combustion is a key factor in the design of a scramjet engine that comprises a fuel injector and combustor.

Knowledge about fuel-air mixing in scramjet combustors, especially the potential for streamwise vorticity to increase the mixing effectiveness beyond that achieved by spanwise vorticity, is summarized in the literature [2–4]. Fernando and Menon [5] showed that a device with a splitter plate leading to streamwise vorticity generation in the mixing layer increased the growth rate of the layer by 380% compared to a normal device without the vorticity generation. Marble *et al.* [6] paid attention to streamwise vorticity generated by the effect of baroclinic torque to enhance the mixing. A previous study [7] has demonstrated that isolated streamwise vortices possess higher unstable properties than flows without axial vorticity. In addition, the importance of vorticity for supersonic fundamental issues should be kept in mind with regard to turbulent transition. For instance, a few studies [8,9] acknowledge that the turbulence level in the streamwise vorticity, i.e., the helicity, can enhance supersonic mixing down to a molecular scale and lead to efficient combustion. Such vortices have the potential to ensure a more uniform distribution of fuel in the combustor. Therefore, there is growing evidence that streamwise vortices are capable of providing not only rapid mixing but also stable combustion in supersonic flows.

The use of streamwise vortex generators for enhancing fuel-air mixing has been studied as described below. Swithenbank *et al.* [10] first investigated the mixing enhancement using a ramped injection configuration that was wall mounted and could generate streamwise vorticities. For such wall-mounted struts, several studies have been conducted using different configurations, including swept and unswept ramp injectors [11,12], staggered ramp injectors [13], and compression and expansion ramps [14]. Moreover, as an alternative to physical ramp injectors, aeroramps, which are multihole transverse injectors that induce pairs of counterrotating vortices to improve mixing and fuel penetration, have been proposed [15]. The aeroramps have similar physical behavior to their physical counterparts, but lower pressure losses and can yield streamwise vortices based on a horseshoe vortex. Furthermore, strut fuel injectors that induce streamwise vortices in the center of the mainstream have also been proposed, including a smooth-lobed strut [16], an alternating wedge strut [8,17,18], a pylon fuel injector [19,20], and a rectangular-lobed strut [21,22].

Although the effect of streamwise vortices on mixing has been studied in terms of the cold flow properties, the role of vortices in combustion is less well known. One of the issues for low flight Mach numbers of a scramjet is autoignition; combustion using streamwise vortices predominates with regard to ignition performance. However, to minimize the heat load of a strut injector, separating the combustion flame from the strut is necessary. In particular, if the trailing edge of each strut, which can introduce streamwise vortices, is too thin, then the attached flame might melt it. In accord with these issues, Gerlinger *et al.* [22] focused on the position of fuel injection and showed that two stable modes of combustion, which are associated with attached and detached flames, depended on the inflow conditions. Eklund *et al.* [23] found that the flow field in the vicinity of the injector was strongly affected by combustion and that the combustion reduced the streamwise vorticity. They also showed that heat release from chemical reactions significantly reduced the mixing between the fuel and airstreams. Thus, it is necessary for supersonic combustion to consider a perspective of interactions between the vortex and combustion. Vortex breakdowns are well known to be effective

*hiejima@aero.osakafu-u.ac.jp

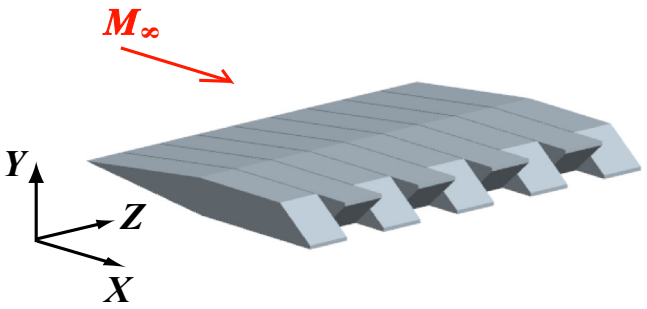

FIG. 1. Schematic diagram of a hypermixer strut.

for flame holding at low-speed flows. The breakdowns are characteristic phenomena linked with streamwise vortices or swirling flows [24,25]. It has been shown without combustion that breakdowns of supersonic streamwise vortices are caused by shock waves [26–28], which might play a useful role in combustion because of the temperature increase behind the shock. Shock waves are necessarily present in a combustor and may influence fuel distributions and combustion; thus, shock-induced combustion on streamwise vortices should be clarified. Furthermore, in achieving a stable combustion in supersonic flows, we have to avoid large subsonic combustion leading to engine unstart as much as possible. The reason is that it leads to severe difficulty in controlling mixing and combustion like that based on boundary layer separation [18]. In this way, one needs to think about more than just strong combustion; to overcome these difficulties, it is essential to elucidate the internal mechanisms of supersonic combustion. In light of previous knowledge, strut fuel injectors located at the combustor center could make it easier to control combustion than wall-mounted struts. The strut injector for inducing streamwise vortices in supersonic flows studied here is shown in Fig. 1.

From a vortex perspective, it is important to gain an understanding of combustion properties. Fundamental phenomena, such as vortex breakdown and shock-vortex interactions, have a critical role in supersonic combustion. Although a number of studies have indicated the potential of streamwise vorticity to increase mixing effectiveness, little is known about the effects of streamwise vortices on combustion and the influences of fuel injection because of the difficulty of working with supersonic flows in the combustion field. The issues have been approached in numerical simulations, as shown in Fig. 2. The purpose of the simulations described in the present report is to investigate the mechanism of the combustion field behind the strut under varying equivalence ratios, focusing on studying the breakdown of the generated streamwise vortical structures and their development in the presence of fuel injections and chemical reactions.

The remainder of this paper is organized as follows. Section II describes the hypermixer strut and combustor geometry. Section III formulates the numerical simulations and states the computational conditions. Section IV provides the results and discusses supersonic combustion related to streamwise vortices at varying equivalence ratios of the injected hydrogen fuel. A summary and conclusions are presented in Sec. V.

II. MODEL AND CONFIGURATION

The computational domain comprises hypermixer struts and combustor geometries used in supersonic combustion tests [18] that were performed at the Japan Aerospace Exploration Agency. The test flow conditions (vitiated airstream and fuel injection) are shown in Table I. The inflow condition for the combustor corresponds to a scramjet flight trajectory at a flight speed of approximately Mach 8. Figure 3(a) shows the combustor from a lateral view; the inflow sectional area is 50×11 mm^2 for the calculated region. The strut is set at the centerline of the combustor, which is 50 mm in height (with an expansion angle of 1.72° with respect to the centerline in the downstream direction). This strut is composed of the leading edge of a symmetry wedge with a half apex angle of 5.7°, the parallel part, and the trailing edge having an asymmetrical upslope and downslope, respectively, which alternate in the spanwise direction: The width of the slope is $D = 11$ mm, the height of the strut is $H = 10$ mm, and the slope angle is θ (deg). The strut can induce streamwise vortices, which are essential in supersonic mixing. Note that the length of the trailing edge $X_S = H/\tan\theta$ shortens with increasing θ. The X-coordinate origin is the trailing edge of the strut and

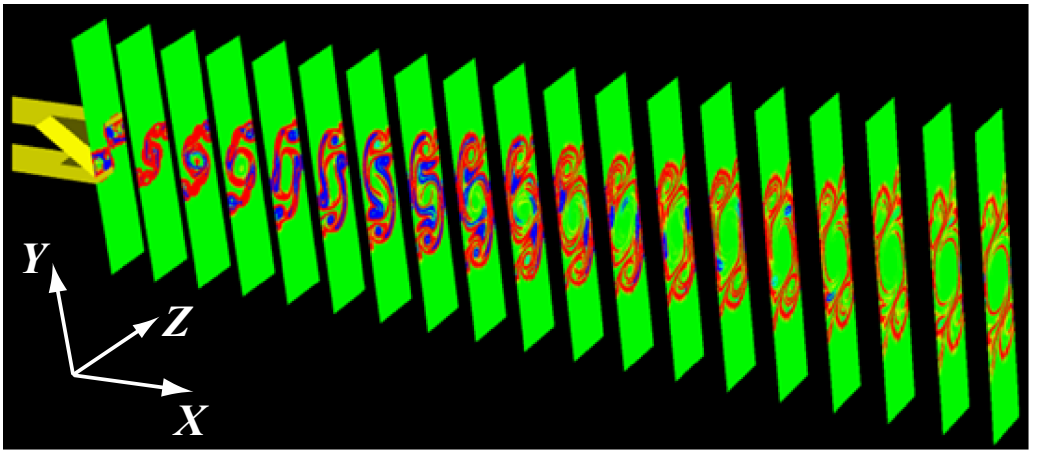

FIG. 2. Contours of the flame index in planes perpendicular to flow behind a hypermixer strut for $\phi = 0.4$ and $\theta = 36°$.

TABLE I. Inflow and fuel injection conditions.

Parameter	Value
Inflow conditions (vitiated airstream)	
Mach number	$M_\infty = 2.48$
velocity	$U_\infty = 1836$ m/s
density	$\rho_\infty = 0.137\,\mathrm{kg/m^3}$
static pressure	$p_\infty = 0.058$ MPa
static temperature	$T_\infty = 1329$ K
N_2 mass fraction	0.524
O_2 mass fraction	0.263
H_2O mass fraction	0.211
OH mass fraction	0.002
unit Reynolds number	$\mathrm{Re_{unit}} = 6.9 \times 10^6\,\mathrm{m^{-1}}$
Fuel injection conditions	
Mach number	$M_{H_2} = 1.0$
velocity	$U_{H_2} = 1300$ m/s
density[a]	$\rho_{H_2} = 0.893\phi\,\mathrm{kg/m^3}$
static pressure[a]	$p_{H_2} = 1.065\phi$ MPa
static temperature	$T_{H_2} = 288.15$ K
fuel mass flow[ab]	$\dot{m}_{H_2} = 0.00444\phi$ kg/s

[a] ϕ denotes the equivalence ratio.
[b] Per two jet orifices.

the coordinate axes are described in Fig. 1. Hydrogen fuel is injected from two jet orifices on the trailing edge ($X = 0$ mm) at sonic speed with an outward angle of 10.24° relative to the centerline in the downstream direction. This contributes to an increment of the vortex circulation due to the vertical velocity component and the avoidance of attached flames, in that the orifice position differs from that in literature [18]. The orifice centers are placed at $Z = \pm 3$ mm; the centerline is at $Z = 0$ mm. The shape of the jet orifice is that of a circle (with a diameter of 2 mm) rubbed into the height of the trailing edge of 1 mm, as in Fig. 3(b).

III. NUMERICAL FORMULATIONS

A. Governing equations

The governing equations are described in Cartesian coordinates x_i ($i = 1$–3) as follows:

$$\frac{\partial \boldsymbol{Q}}{\partial t} + \frac{\partial \boldsymbol{F}_i}{\partial x_i} = \frac{\partial \boldsymbol{F}_{vi}}{\partial x_i} + \boldsymbol{S}, \tag{1}$$

$$\boldsymbol{Q} = \begin{bmatrix} \rho \\ \rho u_1 \\ \rho u_2 \\ \rho u_3 \\ e \\ \rho Y_1 \\ \vdots \\ \rho Y_{ns} \end{bmatrix}, \quad \boldsymbol{F}_i = \begin{bmatrix} \rho u_i \\ \rho u_1 u_i + p\delta_{i1} \\ \rho u_2 u_i + p\delta_{i2} \\ \rho u_3 u_i + p\delta_{i3} \\ (e+p)u_i \\ \rho Y_1 (u_i + V_i^c) \\ \vdots \\ \rho Y_{ns} (u_i + V_i^c) \end{bmatrix},$$

$$\boldsymbol{F}_{vi} = \begin{bmatrix} 0 \\ \tau_{i1} \\ \tau_{i2} \\ \tau_{i3} \\ u_j \tau_{ij} + q_i \\ \rho D_1 \frac{\partial Y_1}{\partial x_i} \\ \vdots \\ \rho D_{ns} \frac{\partial Y_{ns}}{\partial x_i} \end{bmatrix}, \quad \boldsymbol{S} = \begin{bmatrix} 0 \\ 0 \\ 0 \\ 0 \\ 0 \\ \dot{\omega}_1 \\ \vdots \\ \dot{\omega}_{ns} \end{bmatrix}, \tag{2}$$

where $\boldsymbol{Q}$ is a vector of conservative variables, $\boldsymbol{F}_i$ and $\boldsymbol{F}_{vi}$ contain the convective and viscous fluxes, respectively, and $\boldsymbol{S}$ is the chemical source-term vector. Then u_i are the velocity components in Cartesian coordinates and V_i^c is a correction velocity to ensure global mass conservation [29]

$$V_i^c = \sum_{is=1}^{ns} D_k \frac{\partial Y_k}{\partial x_i}. \tag{3}$$

In these expressions,

$$e = \epsilon + \frac{1}{2}\rho u_k u_k, \quad \epsilon = \rho \sum_{is=1}^{ns} Y_{is} h_{is} - p,$$

$$\tau_{ij} = \mu\left(\frac{\partial u_i}{\partial x_j} + \frac{\partial u_j}{\partial x_i} - \frac{2}{3}\delta_{ij}\frac{\partial u_k}{\partial x_k}\right), \tag{4}$$

$$q_i = -\kappa \frac{\partial T}{\partial x_i} + \rho \sum_{is=1}^{ns} D_{is} h_{is} \frac{\partial Y_{is}}{\partial x_i}.$$

Here ϵ is the internal energy, e is the total energy, τ_{ij} is the viscous stress tensor, and q_i is the conductive heat flux. The state equation based on Dalton's law is used to close the system

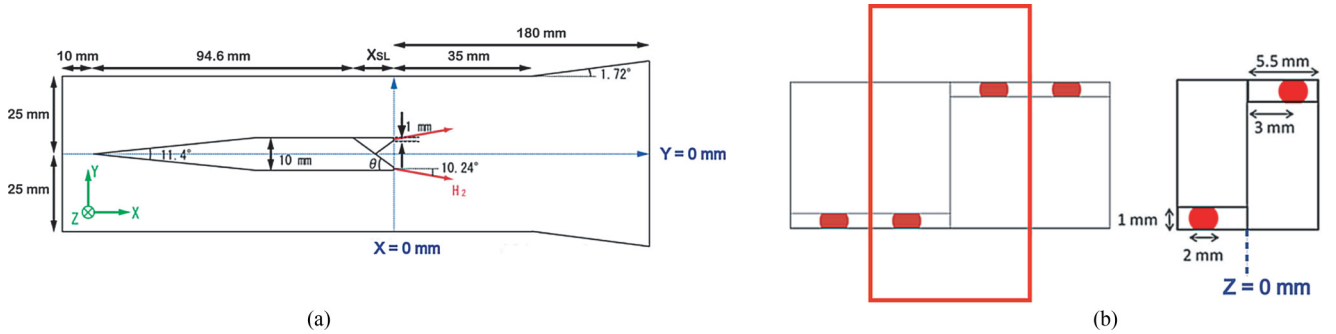

(a) (b)

FIG. 3. Configuration of the computational domain from (a) the lateral view and (b) the rear view; red-filled parts are jet orifices in the trailing edge of the strut injector and the red square denotes the calculated region.

TABLE II. Polynomial coefficient of enthalpy.

Species	$C_{1,is}$	$C_{2,is}$	$C_{3,is}$	$C_{4,is}$	$C_{5,is}$	$C_{6,is}$	$\Delta H^0_{f,is}$
N_2	$-0.943094 \times 10^{-13}$	0.272422×10^{-8}	-0.289382×10^{-4}	0.151090	0.944302×10^{3}	-0.298496×10^{6}	0.000000
O_2	$-0.223197 \times 10^{-12}$	0.432669×10^{-8}	-0.333953×10^{-4}	0.151933	0.857590×10^{3}	-0.269859×10^{6}	0.000000
H_2	0.336925×10^{-11}	-0.512889×10^{-7}	0.226232×10^{-3}	0.462823	0.138548×10^{5}	-0.416431×10^{7}	0.000000
OH	0.681132×10^{-12}	-0.999704×10^{-8}	0.439239×10^{-4}	0.013047	0.170812×10^{4}	-0.518921×10^{6}	0.389870×10^{2}
HO_2	$-0.400629 \times 10^{-12}$	0.839418×10^{-8}	-0.744688×10^{-4}	0.358452	0.905035×10^{3}	-0.300866×10^{6}	0.209200×10^{1}
H_2O	0.559433×10^{-12}	-0.489785×10^{-8}	-0.219514×10^{-4}	0.404153	0.158629×10^{4}	-0.520222×10^{6}	-0.241826×10^{3}
H_2O_2	0.173752×10^{-9}	-0.594331×10^{-6}	0.490390×10^{-3}	0.496788	0.900162×10^{3}	-0.317699×10^{6}	-0.136106×10^{3}
O	$-0.123999 \times 10^{-12}$	0.254815×10^{-8}	-0.118349×10^{-4}	0.020190	0.147218×10^{4}	-0.440858×10^{6}	0.249173×10^{3}
H	$-0.203235 \times 10^{-15}$	0.600278×10^{-11}	-0.571826×10^{-7}	0.000226	0.207856×10^{5}	-0.619730×10^{7}	0.217999×10^{3}

of equations

$$p = \rho R_u T \sum_{is=1}^{ns} \frac{Y_{is}}{\mathcal{M}_{is}}, \tag{5}$$

where p is the static pressure, T is the static temperature, R_u is the universal gas constant, $Y_{is} = \rho_{is}/\rho$ is the mass fraction, and $\mathcal{M}_{is}$ is the molecular weight of the species.

In the present study, the fluid is assumed to be a thermally perfect gas and the thermodynamic quantities for all species are functions of temperature alone. The enthalpy h_{is} can then be calculated using a fifth-order polynomial

$$h_{is}(T) = C_{1,is}T^5 + C_{2,is}T^4 + C_{3,is}T^3 + C_{4,is}T^2 + C_{5,is}T + C_{6,is} + \Delta H^0_{f,is}, \tag{6}$$

where $\Delta H^0_{f,is}$ are the standard enthalpy change of formation under a standard state pressure of 0.1 MPa at 298.15 K and $C_{k,is}$ ($k = 1$–6) are the curve fit constants based on a JANAF table [30], as shown in Table II.

The transport coefficients, including the viscosity μ, the thermal conductivity κ, and the mass diffusions of the species D_{is}, are calculated as follows [31]. The viscosity μ [kg/(m s)] is expressed using the Sutherland-Wassiljewa relation

$$\mu = \sum_{is=1}^{ns} \frac{\mu_{is}}{\sum_{js=1}^{ns} \Phi_{is,js} \frac{X_{js}}{X_{is}}}. \tag{7}$$

The viscosities of the species μ_{is} are obtained using the Chapman-Enskog theory based on the Lennard-Jones intermolecular potential model

$$\mu_{is} = 2.6695 \times 10^{-6} \frac{\sqrt{\mathcal{M}_{is}T}}{\sigma_{is}^2 \Omega_{\mu_{is}}} f_\eta, \tag{8}$$

where $\Omega_{\mu_{is}}$ are the collision integral and $f_\eta \approx 1$. Using the averaged $\Omega_{\mu_{is}}$ in the range of application in temperature, suppose that $\mu_{is} \propto \sqrt{T}$. The collision diameters σ_{is} and the viscous coefficients for species are summarized in Table III. In addition, $\Phi_{is,js}$ are calculated by Wilke's empirical rules

$$\Phi_{is,js} = \frac{\left[1 + \sqrt{\frac{\mu_{is}}{\mu_{js}}}\left(\frac{\mathcal{M}_{is}}{\mathcal{M}_{js}}\right)^{1/4}\right]^2}{\sqrt{8\left(1 + \frac{\mathcal{M}_{is}}{\mathcal{M}_{js}}\right)}}. \tag{9}$$

The mole fractions X_{is} are defined as

$$X_{is} = \frac{\frac{Y_{is}}{\mathcal{M}_{is}}}{\sum_{is=1}^{ns} \frac{Y_{is}}{\mathcal{M}_{is}}}. \tag{10}$$

The thermal conductivity κ [W/(m K)] is obtained from the Sutherland-Wassiljewa relation

$$\kappa = \sum_{is=1}^{ns} \frac{\kappa_{is}}{\sum_{js=1}^{ns} A_{is,js}\left(\frac{X_{js}}{X_{is}}\right) - 0.065}. \tag{11}$$

Here $A_{is,js}$ are given using the Mason-Saxena approximation $A_{is,js} = 1.065\Phi_{is,js}$. The thermal conductivities of the species κ_{is} are given using the Eucken formula in polyatomic gases

$$\kappa_{is} = \mu_{is}\left(C_{p,is} + \frac{5}{4}\frac{R_u}{\mathcal{M}_{is}}\right), \tag{12}$$

where $C_{p,is} = dh_{is}/dT$. For the mass diffusion coefficients of species, the self-diffusion coefficients are applied as $D_{is} = 1.34\,\mu_{is}/\rho$.

A chemical system of ns species reacting through m reactions is described by

$$\sum_{is}^{ns} \nu'_{is,j}[M_{is}] \rightleftharpoons \sum_{is}^{ns} \nu''_{is,j}[M_{is}] \quad \text{for} \quad j = 1, \ldots, m, \tag{13}$$

where $[M_{is}] = \rho Y_{is}/\mathcal{M}_{is}$ and $\nu'_{is,j}$ and $\nu''_{is,j}$ are the molar stoichiometric coefficients of species is in reaction j. The

TABLE III. Collision diameter and viscous coefficient.

Species	σ_{is} (10^{-10} m)	$\mu_{is}/\sqrt{T}$
N_2	3.621	8.688×10^{-7}
O_2	3.548	1.068×10^{-6}
H_2	2.920	3.571×10^{-7}
OH	2.750	1.100×10^{-6}
HO_2	3.458	1.160×10^{-6}
H_2O	2.605	1.160×10^{-6}
H_2O_2	3.458	1.160×10^{-6}
O	3.500	1.150×10^{-6}
H	2.050	3.950×10^{-7}

reaction rates $\dot{\omega}_{is}$ are given by

$$\dot{\omega}_{is} = \mathcal{M}_{is} \sum_{j=1}^{m} (\nu''_{is,j} - \nu'_{is,j}) v_{r,j}, \tag{14}$$

$$v_{r,j} = k_j^f \prod_{i=1}^{ns} \left(\rho \frac{Y_{is}}{\mathcal{M}_{is}} \right)^{\nu'_{is,j}} - k_j^r \prod_{i=1}^{ns} \left(\rho \frac{Y_{is}}{\mathcal{M}_{is}} \right)^{\nu''_{is,j}}, \tag{15}$$

$$k_j^s = A_j T^{\beta_j} \exp\left(-\frac{E_j}{R_u T} \right), \tag{16}$$

where $v_{r,j}$ are the progress rates of reaction j. The rate constants k_j^s are modeled using the empirical Arrhenius law with a constant A_j, a temperature exponent β_j, and an activation energy E_j; then the forward and reverse rates of reaction j are denoted by $s = f$ and $s = r$, respectively. The reaction model used here is that of Westbrook [32], which contains nine species (N_2, O_2, H_2, OH, HO_2, H_2O, H_2O_2, O, and H) and a 17-step reaction mechanism, shown in Table IV.

Equation (1) is transformed into an equation in general coordinates ξ_i (i = 1–3),

$$\frac{\partial \hat{\boldsymbol{Q}}}{\partial t} + \frac{\partial \hat{\boldsymbol{F}}_i}{\partial \xi_i} = \frac{\partial \hat{\boldsymbol{F}}_{vi}}{\partial \xi_i} + \hat{\boldsymbol{S}}, \tag{17}$$

where

$$\hat{\boldsymbol{Q}} = J^{-1} \boldsymbol{Q}, \quad \hat{\boldsymbol{F}}_i = J^{-1} \frac{\partial \xi_i}{\partial x_j} \boldsymbol{F}_j,$$

$$\hat{\boldsymbol{F}}_{vi} = J^{-1} \frac{\partial \xi_i}{\partial x_j} \boldsymbol{F}_{vj}, \quad \hat{\boldsymbol{S}} = J^{-1} \boldsymbol{S},$$

$$J^{-1} = \frac{\partial x_1}{\partial \xi_1} \left(\frac{\partial x_2}{\partial \xi_2} \frac{\partial x_3}{\partial \xi_3} - \frac{\partial x_2}{\partial \xi_3} \frac{\partial x_3}{\partial \xi_2} \right) + \frac{\partial x_1}{\partial \xi_2} \left(\frac{\partial x_2}{\partial \xi_3} \frac{\partial x_3}{\partial \xi_1} - \frac{\partial x_2}{\partial \xi_1} \frac{\partial x_3}{\partial \xi_3} \right) + \frac{\partial x_1}{\partial \xi_3} \left(\frac{\partial x_2}{\partial \xi_1} \frac{\partial x_3}{\partial \xi_2} - \frac{\partial x_2}{\partial \xi_2} \frac{\partial x_3}{\partial \xi_1} \right),$$

with the Jacobian J transforming the coordinate system from physical space to computational space. Then $J^{-1} \partial \xi_i / \partial x_k$ are the derivatives for this coordinate conversion, i.e., the metrics.

B. Numerical methods and computing conditions

To investigate the effects of the streamwise vortices on supersonic combustion using a strut with $\theta = 22^\circ$ and 36°, three-dimensional numerical simulations are conducted for various equivalence ratios ϕ at a Mach number of 2.48 (high-enthalpy flow conditions). The numerical method used here is a kind of shock capturing scheme, because shock waves play an important role in the flow field. The convective flux terms are evaluated by a third-order total variation diminishing scheme [33]. The viscous flux terms are calculated to second-order accuracy by a central difference method. The temporal integration adopts the point-implicit method [34]; using this method, the time step restriction due to the source term, i.e., the time-scale difference between fluid motions and chemical reactions, is relaxed. The computational inlet is located 10 mm upstream of the leading edge of the strut and the outlet is set 180 mm downstream of its trailing edge. For the spanwise direction, the domain comprises the length from half of the down ramp to half of the up ramp, i.e., a streamwise vortex is included. The mesh around the strut is formed by solving the elliptic partial differential equation with regard for orthogonality, with a 232 × 196 × 54 grid. The inflow is fixed to the values in Table I and the outflow condition is extrapolated to zeroth order. Slip conditions are assumed on the up and down walls of the combustor. On the basis of the symmetry shown in Fig. 3(b), the symmetric boundary conditions are applied to the X-Y boundary surfaces in the spanwise direction. The boundary of the strut wall is considered to have unsteady, adiabatic, and no-slip conditions.

To check the resolution, the following results were compared between three grids: grid A (180 × 126 × 50), grid B

TABLE IV. H_2-O_2 reaction model.

		Forward rate f			Reverse rate r		
j	*Reaction*	$\log_{10} A_j$	β_j	E_j	$\log_{10} A_j$	β_j	E_j
1	$H + O_2 \leftrightharpoons O + OH$	14.27	0	16.79	13.17	0	0.68
2	$H_2 + O \leftrightharpoons H + OH$	10.26	1	8.90	9.92	1	6.95
3	$H_2O + O \leftrightharpoons OH + OH$	13.53	0	18.53	12.50	0	1.10
4	$H_2O + H \leftrightharpoons H_2 + OH$	13.98	0	20.30	13.34	0	5.15
5	$H_2O_2 + OH \leftrightharpoons H_2O + HO_2$	13.00	0	1.80	13.45	0	32.79
6	$H_2O + M \leftrightharpoons H + OH + M$[a]	16.34	0	105.00	23.15	−2	0.00
7	$H + O_2 + M \leftrightharpoons HO_2 + M$	15.22	0	−1.00	15.36	0	45.90
8	$HO_2 + O \leftrightharpoons OH + O_2$	13.70	0	1.00	13.81	0	56.61
9	$HO_2 + H \leftrightharpoons OH + OH$	14.40	0	1.90	13.08	0	40.10
10	$HO_2 + H \leftrightharpoons H_2 + O_2$	13.40	0	0.70	13.74	0	57.80
11	$HO_2 + OH \leftrightharpoons H_2O + O_2$	13.70	0	1.00	14.80	0	73.86
12	$H_2O_2 + O_2 \leftrightharpoons HO_2 + HO_2$	13.60	0	42.64	13.00	0	1.00
13	$H_2O_2 + M \leftrightharpoons OH + OH + M$	17.08	0	45.50	14.96	0	−5.07
14	$H_2O_2 + H \leftrightharpoons HO_2 + H_2$	12.23	0	3.75	11.86	0	18.70
15	$O + H + M \leftrightharpoons OH + M$	16.00	0	0.00	19.90	−1	103.72
16	$O_2 + M \leftrightharpoons O + O + M$	15.71	0	115.00	15.67	−0.28	0.00
17	$H_2 + M \leftrightharpoons H + H + M$	14.34	0	96.00	15.48	0	0.00

[a]The symbol M denotes a third body.

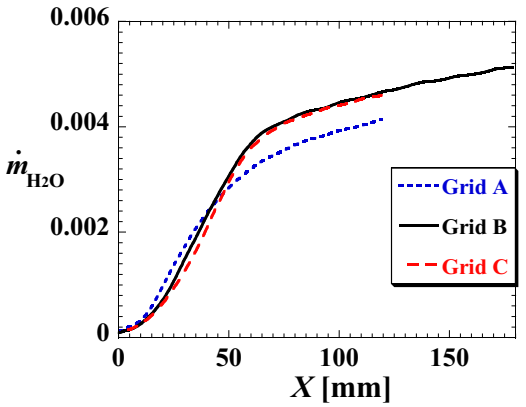

FIG. 4. Water products $\dot{m}_{H_2O}$ integrated in a plane vertical to flow as a function of X.

(232 × 196 × 54), and grid C (343 × 282 × 164). For grids A and C, the computational domains are below $X = 120$ mm. Figure 4 shows the produced-water mass flows integrated in a plane vertical to the mainstream flow as a function of X at $\theta = 36^\circ$ and $\phi = 0.2$. The result for grid A differed from other results, while the difference between grids B and C was small; thus, the resolution of grid B was reasonable in terms of understanding the physical phenomena involved in combustion.

IV. RESULTS AND DISCUSSION

A. Supersonic combustion

The field considered in this study is a flow field with diffusion combustion based on supersonic mixing enhanced by streamwise vortices. To confirm the relationship between mixing and combustion, we compare mixing efficiencies under an equivalence ratio of $\phi = 0.2$ for nonreacting flow with combustion efficiencies for reacting flows at $\theta = 22^\circ$ and 36°, as shown in Fig. 5. For fuel lean flows, the mixing efficiency

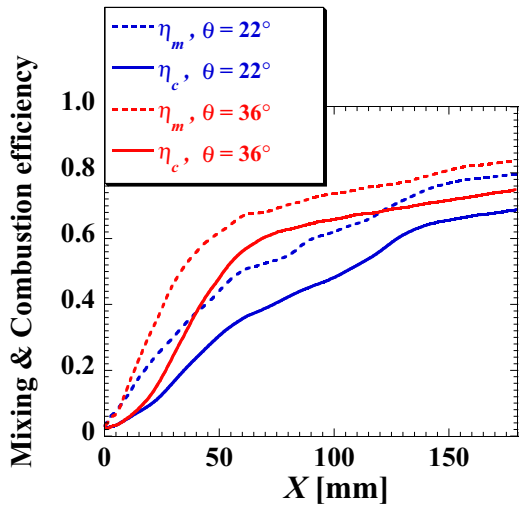

FIG. 5. Mixing efficiency η_m and combustion efficiency η_c for $\phi = 0.2$ at $\theta = 22^\circ$ and 36°.

η_m is defined as [35]

$$\eta_m = \frac{\int_A Y_R \rho u_1 dA}{\int_A Y_{H_2} \rho u_1 dA},$$

$$Y_R = \begin{cases} Y_{H_2} & \text{for} \quad Y_{H_2} \leqslant Y^s_{H_2} \\ Y^s_{H_2}\left(\frac{1-Y_{H_2}}{1-Y^s_{H_2}}\right) & \text{for} \quad Y_{H_2} > Y^s_{H_2}, \end{cases} \tag{18}$$

where Y_{H_2} is the fuel mass fraction, Y_R is the fuel fraction mixed in a proportion that can react, $Y^s_{H_2} = 0.0328$ is the fuel stoichiometric mass fraction, and A is the cross-sectional area in a plane perpendicular to the flow. The combustion efficiency η_c is given by

$$\eta_c = 1 - \frac{\int_A \rho_{H_2} u_1 dA}{\int_A \rho_{H_x} u_1 dA}, \tag{19}$$

$$\rho_{H_x} = \rho_{H_2}\frac{\mathcal{M}_{H_2}}{\mathcal{M}_{H_2}} + \rho_{OH}\frac{\mathcal{M}_H}{\mathcal{M}_{OH}} + \rho_{HO_2}\frac{\mathcal{M}_H}{\mathcal{M}_{HO_2}} + \rho^c_{H_2O}\frac{\mathcal{M}_{H_2}}{\mathcal{M}_{H_2O}} + \rho_{H_2O_2}\frac{\mathcal{M}_{H_2}}{\mathcal{M}_{H_2O_2}} + \rho_H\frac{\mathcal{M}_H}{\mathcal{M}_H},$$

$$\rho^c_{H_2O} = \rho_{H_2O} - \rho_{H_2O,\infty}\frac{\rho_{N_2}}{\rho_{N_2,\infty}}, \tag{20}$$

where $\rho_{H_2O,\infty}$ and $\rho_{N_2,\infty}$ denote the density of H_2O and N_2 under inflow conditions, respectively. Then ρ_{H_x} is expressed as the sum density of hydrogen included in all species. To estimate H_2O generated by combustion, the vitiated airstream H_2O included in the inflow is removed using the nonreactive N_2. Although a slight amount of hydrogen is included with OH in the vitiated airstream, it is not removed. Note that η_m is obtained from the flows without chemical reactions (nonreactive flows) and η_c is obtained from the reactive flows. The case of $\theta = 36^\circ$ indicates faster activity for mixing and combustion than that at $\theta = 22^\circ$. In both the $\theta = 22^\circ$ and 36° cases, the curvilinear features of η_c are similar to those of η_m; thus, the results suggest that the combustion field depends on the mixed control rate.

Figures 6(a) and 6(b) show the contours of the H_2O products obtained from the chemical reaction and the areas of local subsonic Mach number with rendered in red, respectively, in the X-Y cross sections at $\phi = 0.4$ and $\theta = 36^\circ$. Figure 6(a) indicates that supersonic combustion occurs over a relatively wide range in the duct; then the vertical extent of the flame is unchanged beyond $X \approx 110$ mm. Subsonic regions might be generated with combustion because of the increase of the local

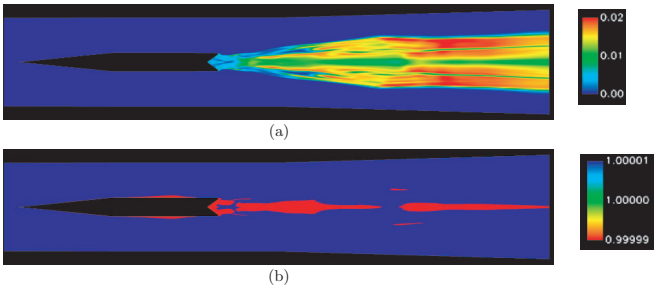

FIG. 6. Contours of (a) H_2O products ρ_{H_2O} and (b) subsonic region rendered in red for $\phi = 0.4$ and $\theta = 36^\circ$ at $Z = 0$ mm.

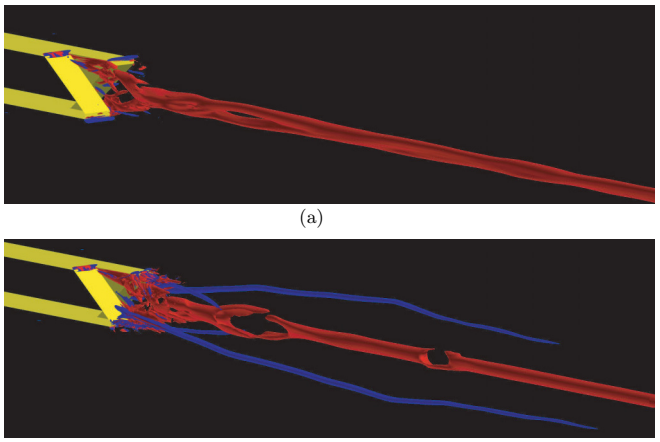

FIG. 7. Isosurface of the second invariant of the velocity gradient tensor Q at $\theta = 36^\circ$ (a) without fuel injection and (b) with fuel injection $\phi = 0.4$. Positive and negative streamwise vorticities are rendered in red and blue, respectively.

sonic velocity resulting from the temperature rise. Without fuel injections, there are only the subsonic regions on the parallel part of the strut due to the reflection of shock waves and in the vicinity of the alternating ramp of the strut due to separation. In Fig. 6(b) subsonic regions increase in size with combustion because two spots on the centerline behind the strut are added to the regions. The cause of strong combustion that is linked to streamwise vortices in the supersonic flow could be attributed to the appearance of the subsonic region. In the present study, the rate of supersonic combustion is high since the extended subsonic regions are smaller than the subsonic zones obtained using the lobed strut [22] at a freestream Mach number ($M_\infty = 2.1$).

B. Vortex breakdown and combustion

From a vortex structure perspective, understanding the effects of fuel injection and combustion on streamwise vortices is worthwhile. To visualize vortical structures, we use the isosurface of the second invariant of the velocity gradient tensor $\mathcal{Q}$ in Fig. 7,

$$\mathcal{Q} = \tfrac{1}{2}(-S_{ij}S_{ij} + R_{ij}R_{ij} + P^2), \tag{21}$$

$$S_{ij} = \frac{1}{2}\left(\frac{\partial u_j}{\partial x_i} + \frac{\partial u_i}{\partial x_j}\right), \quad R_{ij} = \frac{1}{2}\left(\frac{\partial u_j}{\partial x_i} - \frac{\partial u_i}{\partial x_j}\right),$$
$$P = \frac{\partial u_k}{\partial x_k},$$

where S_{ij} and R_{ij} are the strain rate and vorticity tensors, respectively, which denote the symmetric and asymmetric components of the velocity gradient tensor $\partial u_i/\partial x_j$, and P is the divergence of the velocity vectors [36]. In addition, positive and negative streamwise vorticities are rendered in red and blue, respectively, on the isosurfaces. For the case with no fuel injection, shown in Fig. 7(a), a vortex with positive streamwise vorticity was formed by the strut. For $\phi = 0.4$ in Fig. 7(b), negative streamwise vorticities are induced by

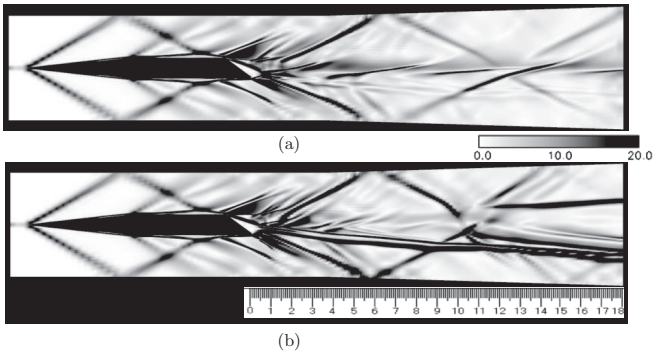

FIG. 8. Schlieren images from a side view at $Z = -5.5$ mm for $\phi = 0.4$ and $\theta = 36^\circ$ (a) without fuel injection and (b) with fuel injection $\phi = 0.4$.

hydrogen injections as added large-scale vortical structures. In contrast to the case with no injections, the streamwise vortex breaks down due to combustion at two positions. These correspond to the subsonic regions caused by the combustion in Fig. 6(b). Vortex breakdown is induced by the interaction between streamwise vortices and shock waves if certain conditions are satisfied [37,38]. Note that vorticity fields in the interaction region are extremely unstable when applied to the effect of hollowness [39] and coherent structures can readily develop around there. Figure 8 shows the contours of the schlieren images in the absence or presence of fuel injection ($\phi = 0.4$) at $Z = -5.5$ mm. The important point is that shock waves cross into the streamwise vortex at $X \simeq 40$ and 105 mm, where vortex breakdowns are observed in Fig. 7(b). The onset of the breakdown depends on the intensity and angle of the impinging shock waves; indeed, the shock intensity and angle increase at the positions where breakdowns and subsonic flows are caused by injection and combustion. In terms of the properties of streamwise vortex breakdown, Di Pierro and Abid [40] indicated that breakdown occurs where the enstrophy ε is close to a maximum in the temporal evolution without combustion,

$$\varepsilon = \int_A \frac{1}{2}\omega_i\omega_i dA, \quad \varepsilon_{y+z} = \varepsilon - \int_A \frac{1}{2}\omega_x^2 dA, \tag{22}$$

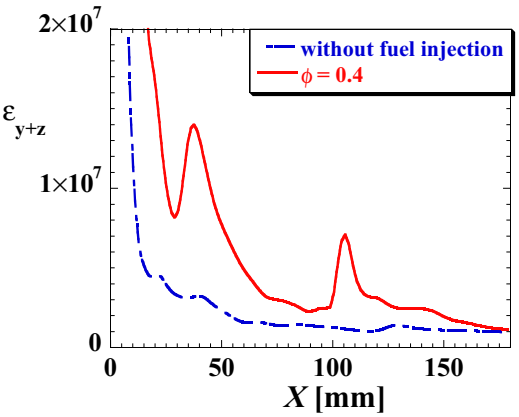

FIG. 9. Spatial development of the enstrophy minus its streamwise vorticity component.

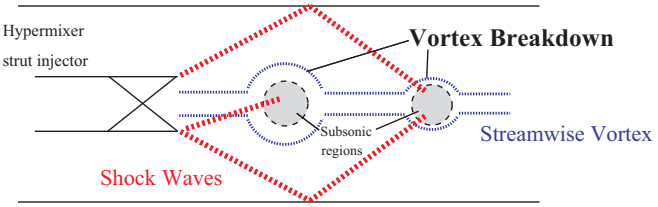

FIG. 10. Schematic of streamwise vortex breakdowns.

where ω_i is a vector of vorticity and A is the cross-sectional area in a plane perpendicular to the flow. Then ε_{y+z} is obtained by subtracting the streamwise vorticity component from the enstrophy. Figure 9 shows ε_{y+z} as a function of X behind the strut with and without fuel injection. The result without fuel injections was dominated by ω_y, due to the boundary layer separation resulting from the slope walls of the strut. The present study found that the breakdowns occurred in the vicinity of the two locations at which ε_{y+z} had local maxima. These are consistent with the results addressed in Fig. 7(b); thus, the variable provides useful information for streamwise vortex breakdown. On the basis of the previous results in this study, Fig. 10 indicates that the mechanism behind supersonic combustion is linked to streamwise vortices. Vortex breakdown requires not only that a shock wave is incident on the streamwise vortices but also that chemical reactions due to temperature increase behind the shock wave. Then, the generated breakdown creates subsonic regions and flame-holding structures. Therefore, vortex breakdown plays an important role in supersonic combustion and the flame holding in the mainstream.

For nonreacting flows [21], it has been reported that the circulation, which describes the strength of the streamwise vorticity, is nearly independent of the equivalence ratio. However, the angle of fuel injection addressed here (see Fig. 3) might contribute to an increase in circulation because of an increase in the vertical velocity component due to the injection direction. Note that even if breakdown of the vortex structure occurs, the total angular momentum is conserved at $X > 0$ when there is a high Reynolds number and when the total enthalpy (or total temperature) is conserved. However, if heat production occurs in the combustion, the conservation of circulation is not necessarily satisfied. To investigate the effect of combustion on streamwise vortices, Fig. 11 plots the circulations under various equivalence ratios ϕ. The circulation of the streamwise vorticity Γ is calculated by

$$\Gamma = \int_A \omega_x dA. \tag{23}$$

For $\theta = 22^\circ$, the circulation decreases with increasing ϕ. However, for $\theta = 36^\circ$, although the circulation is lower than that without injection, Γ for $\phi = 0.6$ and 0.8 become larger than that for $\phi = 0.4$. The reason is that separation occurs on the strut slope at $\theta = 36^\circ$ and the strong injection pressure influences the flow field with the subsonic region near the back of the strut that is related to the formation of streamwise vortices. In essence, the circulation decreases due to the fuel injection, as shown in Appendix B, rather than the increase of the transport coefficients μ, κ, and D_{is} as a result of the temperature increase during combustion. The reduction in streamwise vorticity has been advanced as a possible physical reason for the variation of the field around the strut, which is formed based on the slope angle and the fuel injection. In terms of combustion control, cases such as that with $\theta = 22^\circ$, where circulation depends directly on the equivalence ratio ϕ, are preferred.

C. Flame structures for streamwise vortices

Figure 12 shows the contours of streamwise vorticity ω_x, hydrogen density ρ_{H_2}, and heat release Q_{HR} at six different X positions. In Fig. 12(a), positive and negative streamwise vorticities are rendered in white and black, respectively. The

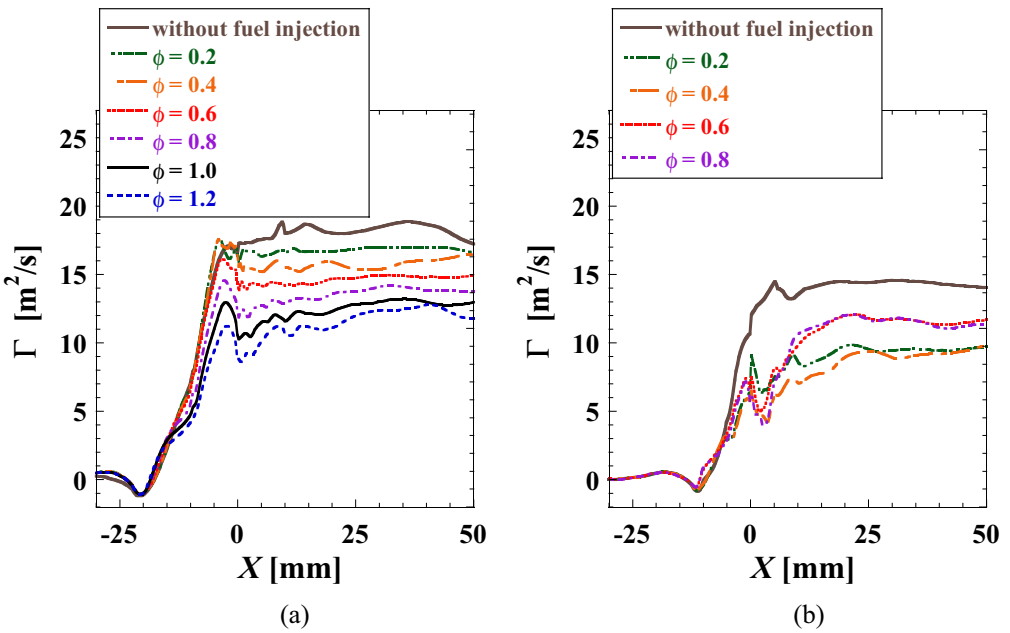

FIG. 11. Streamwise variations in circulations for various equivalence ratios at (a) $\theta = 22^\circ$ and (b) $\theta = 36^\circ$.

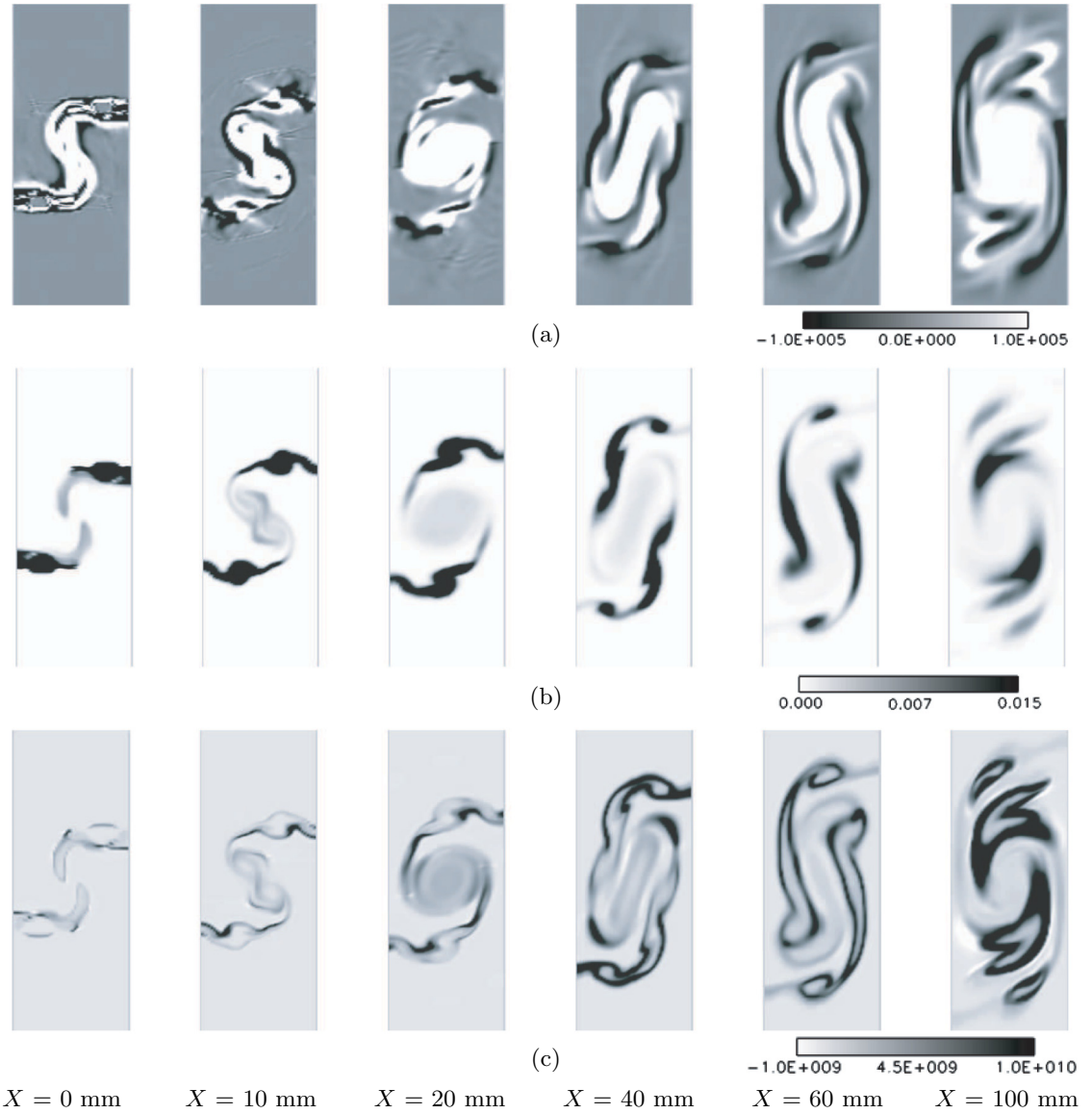

FIG. 12. Contours of (a) streamwise vorticities ω_x, (b) hydrogen densities ρ_{H_2}, and (c) heat releases Q_{HR} in various planes vertical to the mainstream flow at $\theta = 22^\circ$ and $\phi = 0.4$.

process of streamwise vortex formation is similar to that without fuel injections for $X < 10$ mm, unlike the case where there is injection into the core region of the vortex using the same strut with a fuel-injector orifice on the intersection of an upslope and a downslope [17,18,41]. For $\theta = 22^\circ$ and $\phi = 0.4$, the injection from the trailing edge has a small effect on the flow in the slope part, which forms a streamwise vortex. When $\theta = 22^\circ$, although ω_x is entirely positive without fuel injection, negative streamwise vorticities occur due to the injection and contribute to mixing [42,43] at the interface between the fuel, H_2, and the airstream. In Figs. 12(b) and 12(c), the number of variables is gradated from white (small) to black (large). The fuel, H_2, is taken in the streamwise vortex by the entrainment effect of the vortex. The contact interface between H_2 and the air is vertically elongated along the outline of the formed vortex. The H_2 distributions are compatible with the vortex region, including the domain consumed by combustion. Moreover, the unburnt H_2 is not found in the center of vortex. This feature differs from the result of the case where H_2 is injected from the trailing edge (all the rear-wall surface) of a lobed strut [21]. The difference is related to the presence or absence of fuel injection in the vortex core region. Gerlinger *et al.* [22] also showed that both η_m and η_c are high where the injection takes place away from the axis of the formed vortex. However, since η_c decreases with increasing ϕ, their result is simply based on the difference of ϕ. In the combustion field, heat-release distributions should be understood to be involved in forming streamwise vorticities. Eklund *et al.* [23] indicated that heat release reduced mixing based on the difference between η_m and η_c. Heat release Q_{HR} is defined as

$$Q_{HR} = -\sum_{is=1}^{ns} h_{is}\dot{\omega}_{is}. \tag{24}$$

The Q_{HR} region corresponds to the outline of the domain wherein H_2 exists and strong heat release appears in the

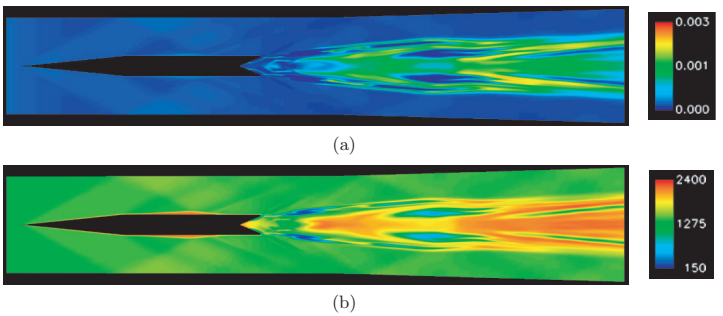

FIG. 13. Contours of (a) OH products ρ_{OH} and (b) static temperature T for $\phi = 0.4$ and $\theta = 22^{\circ}$ at $Z = 0$ mm.

vicinity of high concentrations of H_2. Such a heat release exists in the form of laminae in the vortex; thus, a proper reaction form is maintained. Figure 13 shows the contours of OH products ρ_{OH} and static temperature T at $Z = 0$ mm for $\phi = 0.4$ and $\theta = 22^{\circ}$. Since OH distributions appear with the heat release and the low-temperature domain of fuel is presented just behind the strut, the flame is found to be detached from the strut. This becomes a stable combustion because there is a high-temperature region with detached flames held in place by shock waves and subsonic regions.

To understand the flame structure in a streamwise vortex, we deal with the time-averaged data at $\theta = 22^{\circ}$ and $\phi = 0.8$ and show the analysis contours in Fig. 14. Although the flames are usually unsteady, they remain stationary as a whole. Yamashita *et al.* [44] proposed two parameters to interpret the structure of flames. The first is the mixedness Z_{FO} defined as

$$Z_{FO} = \begin{cases} \frac{Y_{\mathrm{O}_2}}{J_M} & \text{for} \quad \frac{Y_{\mathrm{O}_2}}{J_M} \leqslant Y_{\mathrm{H}_2} \\ -Y_{\mathrm{H}_2} & \text{for} \quad \frac{Y_{\mathrm{O}_2}}{J_M} > Y_{\mathrm{H}_2}, \end{cases} \tag{25}$$

where $J_M = \frac{\mathcal{M}_{\mathrm{O}_2}\nu_{\mathrm{O}_2}}{\mathcal{M}_{\mathrm{H}_2}\nu_{\mathrm{H}_2}}$. Positive and negative values of Z_{FO} denote fuel-rich and fuel-lean mixtures, respectively. The region rendered in red represents the rich fuel H_2. In Fig. 14(a) we can confirm from the result that there is no hydrogen in the center of the streamwise vortex. This suggests that mixing and the consumption of H_2 are enhanced there. The other parameter is the flame index G_{FO}, which distinguishes premixed flames from diffusion flames and is defined as

$$G_{FO} = \nabla Y_{\mathrm{H}_2} \cdot \nabla Y_{\mathrm{O}_2}. \tag{26}$$

Positive and negative values of G_{FO} denote premixed and diffusion flames, respectively; then diffusion and premixed flames are rendered in red and blue. The premixed region indicates a high mixed area. Figure 14(b) indicates that premixed flames occur in the vortex core and in the vortical structures generated by the injections [see Fig. 7(b)]. As is also known from a lateral view at $Z = 0.0$ mm in Fig. 15, for $\theta = 22^{\circ}$, premixed flames accompanied by H_2 entrained in a streamwise vortex appear at $X > 20$ mm [see Fig. 14(b)].

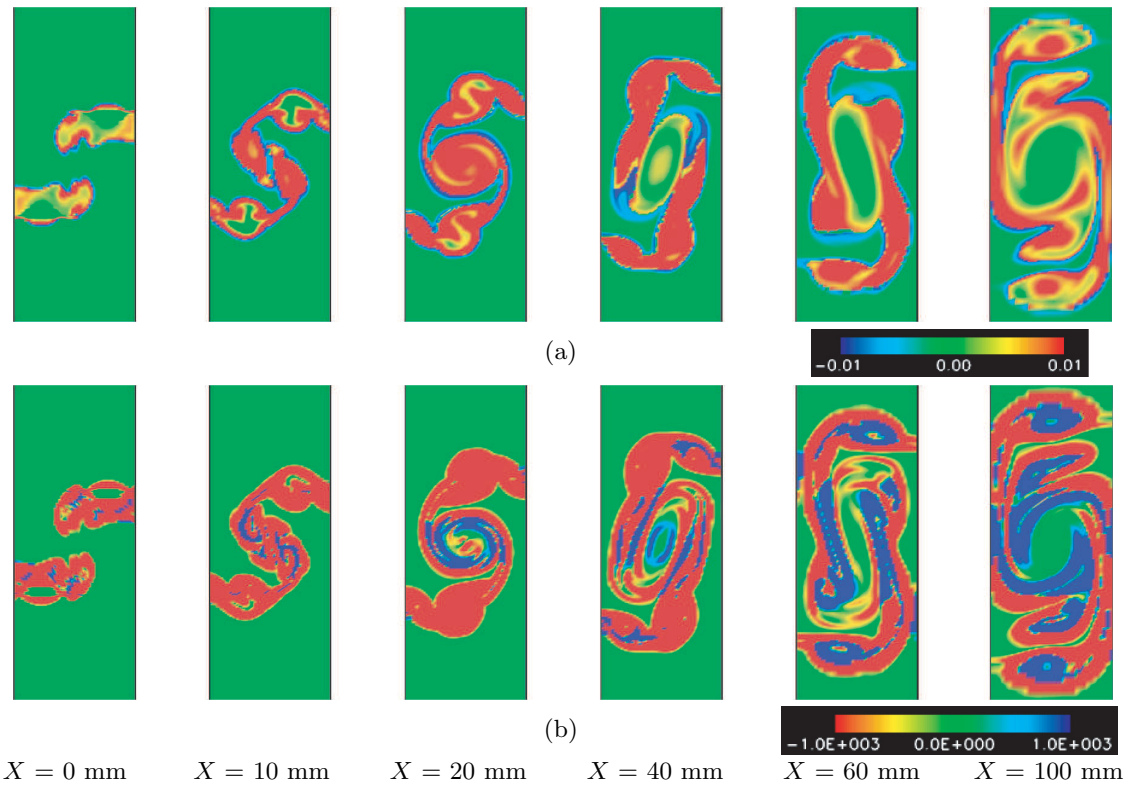

FIG. 14. Contours of (a) mixedness Z_{FO} and (b) flame index G_{FO} in various planes vertical to the mainstream flow at $\theta = 22^{\circ}$ and $\phi = 0.8$.

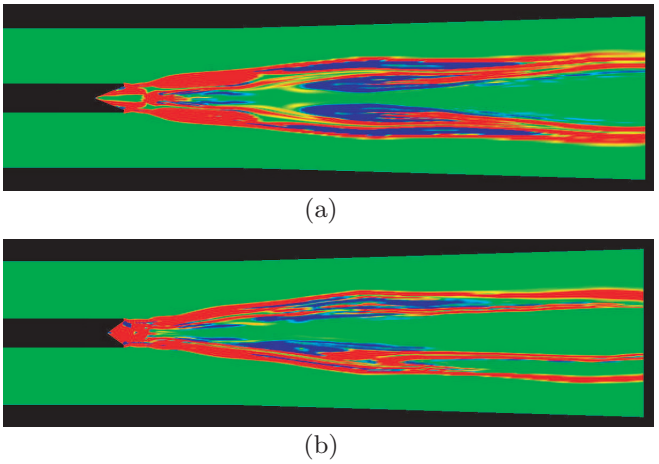

FIG. 15. Contours of flame index for $\phi = 0.8$ at $Z = 0$ mm and (a) $\theta = 22^\circ$ and (b) $\theta = 36^\circ$.

Similarly, for $\theta = 36^\circ$, premixed flames occur in the vortex. Although the field is dominated by diffusion flames, one characteristic is that premixed flames are generated in the streamwise vortex. From the results, we deduce that the flame is involved in forming a stable combustion field. As illustrated in Figs. 12 and 14, the hydrogen fuel is effectively elongated by the entrainment effect of the streamwise vortex such that the contact area between the fuel and the oxygen in the stream is enhanced and the laminated flame structures are formed in the vortex. The schematic is shown in Fig. 16. These behaviors occur in a plane vertical to the supersonic mainflow, relaxing compressibility effects. It follows that the fuel injection used in this study is suitable for supersonic combustion.

D. Supersonic combustion properties

When ϕ is small, the combustion coefficient η_c is large. However, high η_c does not automatically mean a good combustion, i.e., a high combustion pressure. To understand the features of combustion, we introduce the combustion property $\mathcal{Q}_\phi$, defined as the product of the total equivalence ratio and the combustion coefficient

$$\mathcal{Q}_\phi = \eta_c \phi. \tag{27}$$

The mass flow of H_2O in Eq. (20), which is generated by combustion, in a plane perpendicular to the flow is given by

$$\dot{m}_{H_2O} = \int_A \rho^c_{H_2O} u_1 dA. \tag{28}$$

Figure 17 shows comparisons between the combustion property $\mathcal{Q}_\phi$ and the produced-water mass flow $\dot{m}_{H_2O}$ in streamwise variation for various values of ϕ. The combustion intensity increases with ϕ. Although the cases with $\theta = 36^\circ$ indicate faster burning than those with $\theta = 22^\circ$, the former growth rate has a tendency to be saturated. For both $\theta = 22^\circ$ and 36°, the curvilinear features of $\mathcal{Q}_\phi$ coincide with those of $\dot{m}_{H_2O}$ that indicate the net amount of combustion. On the basis of this valuable result, we can compare the obtained results with others from the literature using the combustion property defined above.

Using the formula (27) proposed here, Fig. 18 plots the numerical results at $X = 180$ mm and many data sets (experimental [12,45] and numerical [23] results) concerning

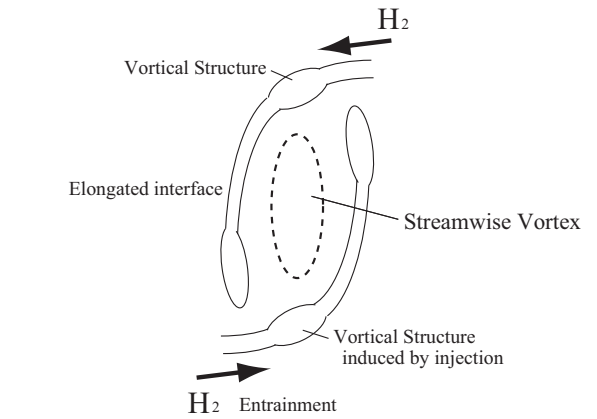

FIG. 16. Schematic of the entrainment process of H_2 due to a streamwise vortex.

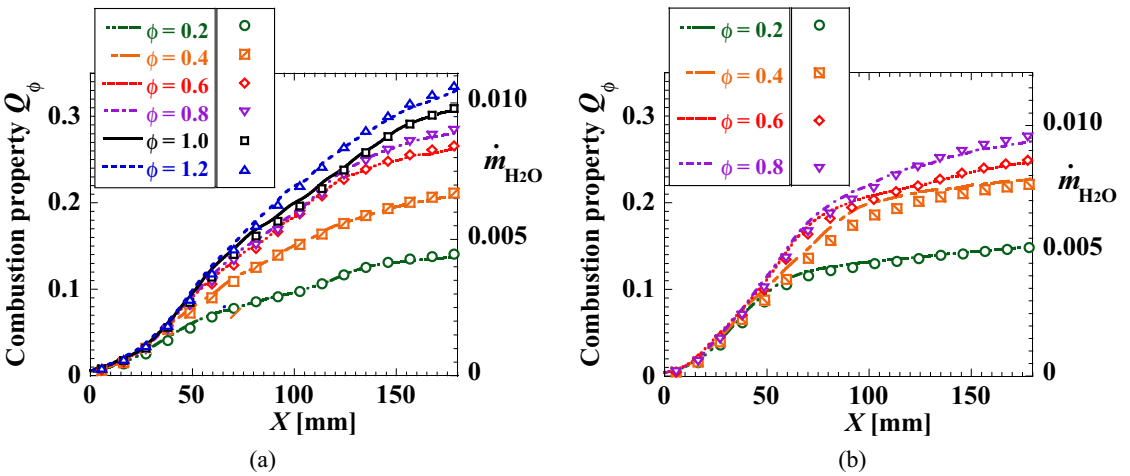

FIG. 17. Streamwise variations in combustion properties $\mathcal{Q}_\phi$ and produced-water mass flows $\dot{m}_{H_2O}$ for various equivalence ratios at (a) $\theta = 22^\circ$ and (b) $\theta = 36^\circ$.

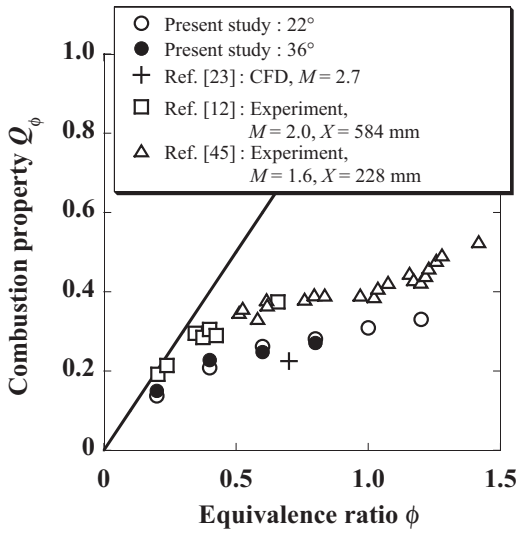

FIG. 18. Combustion property $\mathcal{Q}_\phi$ vs equivalence ratio ϕ.

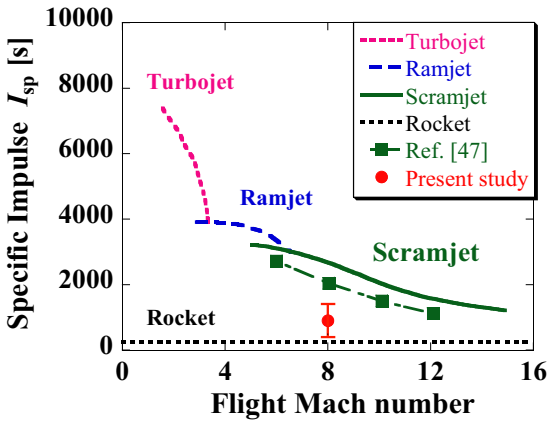

FIG. 19. Specific impulse I_{sp} as a function of the flight Mach number for hydrogen-fueled engines.

strut-injectors. The solid line demonstrates an ideal state with $\eta_c = 1$. The results of $\theta = 22°$ differ little from those of $\theta = 36°$. For every ϕ, the $\mathcal{Q}_\phi$ obtained here is lower than that in experiments with wall-mounted swept ramp injectors [12,45]. The reason is that the present Mach number differs from them and the simulation addresses laminar flow. However, the present study at $M_\infty = 2.48$ compares favorably with the literature [23] using turbulent models at $M_\infty = 2.7$ and is similar to the experiments at $M_\infty = 1.6$–2.0 in terms of the qualitative trend of the equivalence ratio. In addition, Fig. 18 indicates that the amount of combustion has a tendency to decrease with increasing mainstream Mach number. This also conforms to the fact that diffusion combustion is significantly affected by compressibility effects suppressing the mixing activity. In particular, the important thing is that the combustion property is saturated at $\phi > 0.4$, although a slight increase occurs at $\phi \approx 1$. For $M_\infty = 2.8$, Rust *et al.* [21] stated that their single-wedge lobed strut could achieve a perfect mixing and combustion at $\phi = 0.4$. Although they did not present η_c, their result is not inconsistent with the property in Fig. 18. Thus, we can estimate supersonic combustion using the $\mathcal{Q}_\phi$ proposed here.

In fact, it is important to know how thrust is obtained by supersonic combustion. Since the up and down walls on combustor are assumed to be slip walls, the thrust F_T is calculated from the momentum as follows:

$$F_T = -\iint_S (\rho u_i u_j + p\delta_{ij}) n_k dS_k, \tag{29}$$

where the control surface S is the surface area of the domain in Fig. 3(a) and n_k is a normal vector on the surface. Note that F_T includes the drag working on the strut injector because of the integral value in the control surface. The specific impulse I_{sp} is

$$I_{sp} = \frac{F_T}{\dot{m}_{H_2} g}. \tag{30}$$

Figure 19 compares the obtained results with ideal analytical curves for hydrogen-fueled engines [46] included in Smart's recent analysis [47]. So far, an estimation of propulsion performance based on three-dimensional simulations has never been conducted. As described before, the present study deals with combustor inlet conditions, which correspond to a flight Mach number of approximately 8. Naturally, the present value ($I_{sp} = 500$–1400 s) is low compared with that from the one-dimensional ideal analysis with $\eta_c = 1$ and the feature corresponds to the result of the combustion property in Fig. 18. Considering that the net thrust should be a little larger, it follows that the value is within the acceptable range. However, it is necessary for the thrust increase to improve the gain when ϕ is large.

V. CONCLUSION

Several hypermixer strut injectors have achieved supersonic combustion using streamwise vorticity induced by the strut [12,17,23,45]. However, the effects of the streamwise vorticity on combustion are less well understood. In addition, whether the flow field with the streamwise vorticity is affected by fuel injection is unknown. The major reason is that it is difficult to resolve the combustion field in experiments. This study investigated the combustion flow field with a streamwise vortex and hydrogen injections for various ϕ at Mach number 2.48, which corresponded to a flight speed of Mach 8. For a combustor with strut injectors, the mechanism of combustion with streamwise vortices was elucidated under a variety of equivalence ratios. The results showed that the burning behavior was effectively enhanced at the point at which shock waves were incident on the vortex. Then, at points fixed in the shock, the vortex breakdown in the subsonic regions was caused by combustion and the domains in the mainstream led to the formation of stable combustion fields. This contrasted with the combustion that occurred in subsonic regions on the wall, where the flame could go back upstream everywhere through the boundary layer, as a form of unstable combustion. In fact, the interaction between shock waves and the streamwise vortices induced by the strut formed flame-holding regions due to vortex breakdowns suited to combustion in the mainstream flow. Therefore, it followed that the streamwise vortex breakdown had an essential role in combustion enhancement and flame holding under supersonic inflow conditions. Furthermore, it was shown that

the combustion property $\mathcal{Q}_\phi$ defined here coincided with the produced-water mass flow and was a useful variable wherein combustion was evaluated by comparison with other results from the literature. For the Mach number 2.48, combustion occurred partially in subsonic regions. Hereafter, it is necessary to enhance the combustion efficiency at a high equivalence ratio and to investigate whether pure supersonic combustion may occur at higher Mach numbers ($M_\infty > 2.5$) increasing the compressibility effects in terms of a high flight Mach number.

ACKNOWLEDGMENTS

The author is deeply grateful to Emeritus Prof. M. Nishioka and S. Ueyama for fruitful information in considering the computational code of nonequilibrium reacting gas flows and thanks T. Oda, Y. Maeoka, and T. Ono for their assistance in addressing the numerical simulations and its postprocessing. He expresses his gratitude to the anonymous referees for helping to improve the paper.

APPENDIX A: EXTREMUM CONDITION OF ENSTROPHY AND VORTEX BREAKDOWN SHAPES

The enstrophy condition used in Sec. IV B is derived from incompressible equations [40]. Using compressible terms in vorticity equation, the effect of compressibility on the condition is investigated, because the baroclinic torque term is generally crucial in supersonic flows. The vorticity equation is given by

$$\frac{D\boldsymbol{\omega}}{Dt} = \underbrace{(\boldsymbol{\omega}\cdot\nabla)\boldsymbol{u}}_{I}\underbrace{-\boldsymbol{\omega}(\nabla\cdot\boldsymbol{u})}_{II} + \underbrace{\frac{\nabla\rho\times\nabla p}{\rho^2}}_{III} + (\text{transport coefficient terms}), \tag{A1}$$

where $\boldsymbol{u}$ and $\boldsymbol{\omega}$ denote the velocity and vorticity vectors, respectively. Terms I, II, and III specify the stretching, dilatation, and baroclinic torque, respectively. Terms II and III are unique to compressible flows. The effect of transport coefficient terms is not large in high-speed flows. Figure 20 plots terms I–III integrated over the cross-sectional area perpendicular to the X direction in the absence or presence of fuel injection ($\phi = 0.4$). Although term III has no effect on the flow, term II is involved in the vicinity of $X \approx 105$ mm. Thus, the extremum condition is linked to vortex breakdown at $X \approx 40$ mm, but the condition is not satisfied at $X \approx 105$ mm, because there is a possibility that the large change is caused by a strong shock wave. However, the correlation between the extremum position and the breakdown location is also shown in supersonic streamwise vortices [42]. The local maximum value in Eq. (22) provides a useful perspective in compressible flows. Subsonic regions are strongly linked with vortex breakdown and combustion. The large change of terms I and II in Fig. 20 correlates with the increased subsonic parts in Fig. 6(b).

Since vortex breakdown occurs when the vortex interacts with shock waves [37], it is very important to deduce the vortex breakdown shape in this study. In vortex breakdown experiments, literatures [48–50] show the two shapes: Spiral-type vortex breakdowns are related to an axial strain and

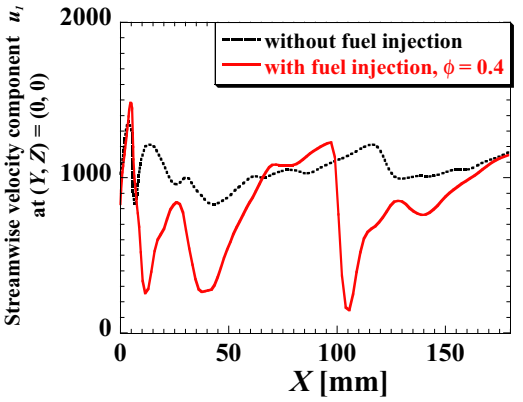

FIG. 21. Streamwise velocity component u_1 at the vortex center $(Y,Z) = (0,0)$ without fuel injection and with fuel injection $\phi = 0.4$ at $\theta = 36^\circ$.

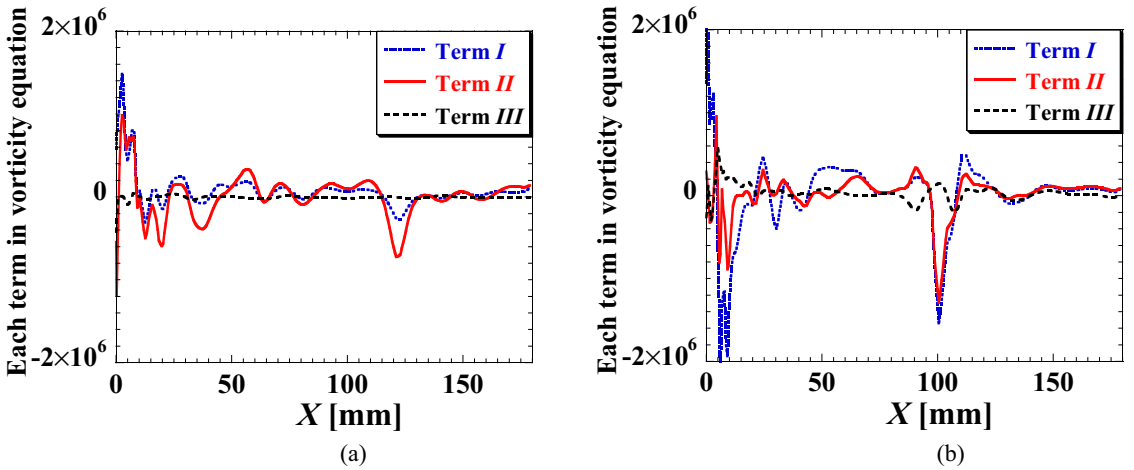

FIG. 20. Terms I–III in the vorticity equation (A1) integrated over the cross-sectional area perpendicular to the X direction (a) without fuel injection and (b) with fuel injection $\phi = 0.4$ at $\theta = 36^\circ$.

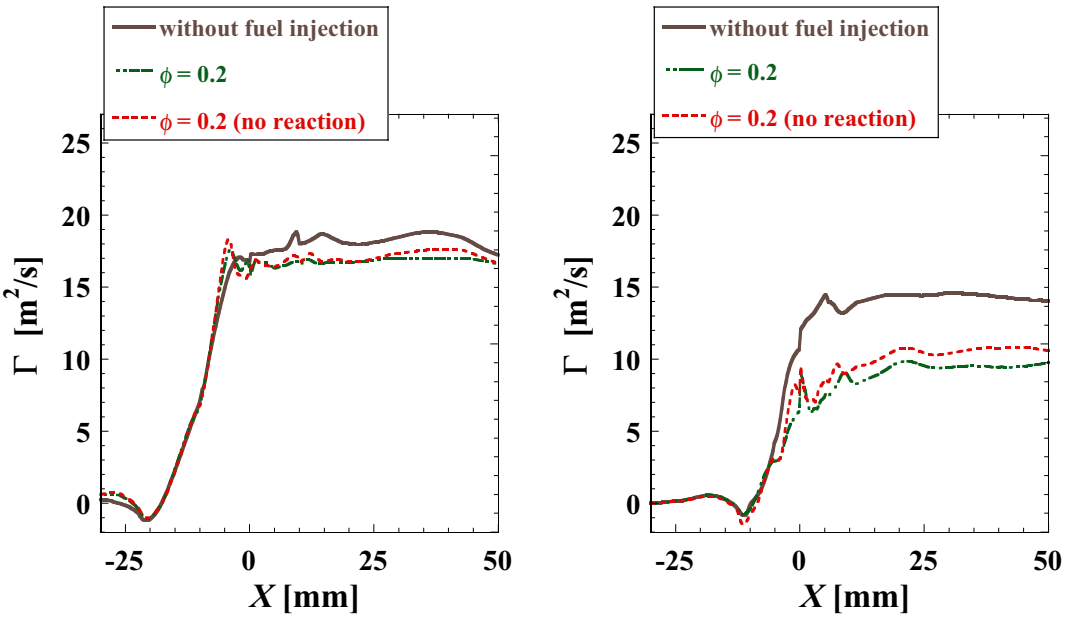

FIG. 22. Streamwise variations in circulations without fuel injection, with reacting and nonreacting flows ($\phi = 0.2$) at (a) $\theta = 22^\circ$ and (b) $\theta = 36^\circ$.

bubble-type vortex breakdowns occur due to the presence of a stagnation point. As shown in Fig. 20(b), terms *I* and *II* in Eq. (A1), which are related to the strain, have a small impact on the vorticity at $X \approx 40$ mm, while they have a large effect at $X \approx 105$ mm. To check a stagnation point, streamwise velocities u_1 at the vortex center are shown in Fig. 21, without fuel injection and with fuel injection $\phi = 0.4$ at $\theta = 36^\circ$. The streamwise velocity deficit without fuel injection is found to be large because of $U_\infty = 1836$ m/s; this condition is likely to give birth to vortex breakdown induced by shock. The extremum of velocity at $X \approx 10$ may be linked to shock-wave angles affected by the combustion. The velocities on both the extremum positions in Fig. 9 are greatly decreased by combustion, but they do not lead to the generation of the stagnation point. Therefore, both breakdowns that occur in Fig. 7(b) are of spiral type.

APPENDIX B: REDUCTION IN STREAMWISE VORTICITY WITH FUEL INJECTION AND COMBUSTION

Since the hydrogen round jet itself can produce streamwise vorticity, the reduction in streamwise vorticity is open to question. Figure 22 shows the circulations of streamwise vorticity without fuel injection, with a reacting flow and nonreacting flow at $\phi = 0.2$, where the mixing and combustion efficiencies are high. For $\theta = 22^\circ$, there is little difference between a reacting and nonreacting flows in circulation and for $\theta = 36^\circ$ there is a little effect of combustion based on faster activity for mixing due to separation on the strut wall. In both the cases, the injection has a large influence on the formation of streamwise vorticity (it discourages a large-scale streamwise vortex formed from the strut). Thus, it follows that the effect of injection on the circulation is large and the effect of combustion and heat release is small here.

[1] F. S. Billig, J. Propul. Power **9**, 499 (1993).
[2] G. S. Settles, NASA Report No. CR-188920, 1991.
[3] E. J. Gutmark, K. C. Schadow, and K. H. Yu, Annu. Rev. Fluid Mech. **27**, 375 (1995).
[4] E. T. Curran, W. H. Heiser, and D. T. Pratt, Annu. Rev. Fluid Mech. **28**, 323 (1996).
[5] E. M. Fernando and S. Menon, AIAA J. **31**, 278 (1993).
[6] F. E. Marble, G. J. Hendricks, and E. E. Zukoski, AIAA Report No. 87, 1987.
[7] T. Hiejima, Phys. Fluids **25**, 114103 (2013).
[8] M. Nishioka *et al.*, in *Proceedings of the IUTAM Symposium on Elementary Vortices and Coherent Structures: Significance in Turbulence Dynamics* (Springer, Berlin, 2006), pp. 249–258.
[9] A. Ingenito and C. Bruno, AIAA J. **48**, 515 (2010).
[10] J. Swithenbank *et al.*, AIAA Report No. 89, 1989.
[11] D. W. Riggins and P. H. Vitt, J. Propul. Power **11**, 419 (1995).
[12] G. B. Northam *et al.*, J. Propul. Power **8**, 491 (1992).
[13] J. P. Drummond, AIAA J. **52**, 465 (2014).
[14] T. Arai *et al.*, AIAA Report No. 2006, 2006.
[15] R. P. Fuller *et al.*, J. Propul. Power **14**, 135 (1998).
[16] I. A. Waitz *et al.*, Prog. Aerosp. Sci. **33**, 323 (1997).
[17] T. Sunami, N. M. Wendt, and M. Nishioka, AIAA Report No. 98, 1998.
[18] T. Sunami *et al.*, AIAA Report No. 2002, 2002.
[19] J. C. Doster *et al.*, J. Propul. Power **25**, 885 (2009).
[20] L. Maddalena, F. Vergine, and M. Crisanti, Phys. Fluids **26**, 046101 (2014).

[21] B. Rust, P. Gerlinger, and M. Aigner, AIAA Report No. 2010, 2010.
[22] P. Gerlinger *et al.*, Aerosp. Sci. Technol. **12**, 159 (2008).
[23] D. R. Eklund, S. D. Stouffer, and G. B. Northam, J. Propul. Power **13**, 697 (1997).
[24] O. Lucca-Negro and T. O'Doherty, Prog. Energy Combust. Sci. **27**, 431 (2001).
[25] S. Leibovich, AIAA J. **22**, 1192 (1984).
[26] J. M. Delery, Prog. Aerosp. Sci. **30**, 1 (1994).
[27] L. N. Cattafesta and G. S. Settles, AIAA Report No. 92, 1992.
[28] I. M. Kalkhoran and M. K. Smart, Prog. Aerosp. Sci. **36**, 63 (2000).
[29] T. Poinsot and D. Veynante, *Theoretical and Numerical Combustion*, 2nd ed. (Edwards, Philadelphia, 2005).
[30] M. W. Chase, Jr., C. A. Davies, J. R. Downey, Jr., D. J. Frurip, R. A. Mc Donald, and A. N. Syverud, in *JANAF Thermochemical Tables*, 3rd ed., special issue of J. Phys. Chem. Ref. Data Suppl. 1 **14** (1985).
[31] R. C. Reid, J. M. Prausnitz, and B. E. Poling, *The Properties of Gasses and Liquid*, 4th ed. (McGraw-Hill, New York, 1987).
[32] C. K. Westbrook, Combust. Sci. Technol. **29**, 67 (1982).
[33] S. R. Chakravathy and S. Osher, AIAA Report No. 85, 1985.
[34] H. C. Yee, NASA Report No. 101088, 1989.
[35] M. Mao, D. W. Riggins, and C. R. McClinton, NASA CP-3078, pp. 635–667, 1991.
[36] J. Jeong and F. Hussain, J. Fluid Mech. **285**, 69 (1995).
[37] T. Hiejima, Phys. Rev. E **89**, 053017 (2014).
[38] M. K. Smart, I. M. Kalkhoran, and S. Popovic, Shock Waves **8**, 243 (1998).
[39] T. Hiejima, Phys. Fluids **28**, 044104 (2016).
[40] B. Di Pierro and M. Abid, Phys. Fluids **23**, 025104 (2011).
[41] M. Kodera and T. Sunami, in *Proceedings of the International Workshop on Future of CFD and Aerospace Sciences, Kobe, Japan, 2012*, http://www.ifs.tohoku.ac.jp/edge/fny60/index.html.
[42] T. Hiejima, Phys. Fluids **26**, 074102 (2014).
[43] T. Hiejima, Phys. Fluids **27**, 034103 (2015).
[44] H. Yamashita, M. Shimada, and T. Takeno, in *Proceedings of 26th International Symposium on Combustion* (Elsevier, Amsterdam, 1996), pp. 27–34.
[45] S. D. Stouffer *et al.*, AIAA Report No. 93, 1993.
[46] L. Maurice, T. Edwards, and J. Griffiths, in *Scramjet Propulsion*, edited by E. T. Curran and S. N. B. Murthy (AIAA, Reston, 2001), Vol. 189, pp. 757–822.
[47] M. K. Smart, AIAA J. **50**, 610 (2012).
[48] Y. Cuypers, A. Maurel, and P. Petitjeans, Phys. Rev. Lett. **91**, 194502 (2003).
[49] M. P. Escudier, Exp. Fluids **2**, 189 (1984).
[50] H. J. Lugt, *Introduction to Vortex Theory* (Vortex Flow, Potomac, 1997).